

Multi-View Wireless Sensing via Conditional Generative Learning: Framework and Model Design

Ziqing Xing, Zhaoyang Zhang, Zirui Chen, Hongning Ruan, and Zhaojun Yang

Abstract—In this paper, we incorporate physical knowledge into learning-based high-precision target sensing using the multi-view channel state information (CSI) between multiple base stations (BSs) and user equipment (UEs). Such kind of multi-view sensing problem can be naturally cast into a conditional generation framework. To this end, we design a bipartite neural network architecture, the first part of which uses an elaborately designed encoder to fuse the latent target features embedded in the multi-view CSI, and then the second uses them as conditioning inputs of a powerful generative model to guide the target's reconstruction. Specifically, the encoder is designed to capture the physical correlation between the CSI and the target, and also be adaptive to the numbers and positions of BS-UE pairs. Therein the view-specific nature of CSI is assimilated by introducing a spatial positional embedding scheme, which exploits the structure of electromagnetic(EM)-wave propagation channels. Finally, a conditional diffusion model with a weighted loss is employed to generate the target's point cloud from the fused features. Extensive numerical results demonstrate that the proposed generative multi-view (Gen-MV) sensing framework exhibits excellent flexibility and significant performance improvement on the reconstruction quality of target's shape and EM properties.

Index Terms—Integrated sensing and communication (ISAC), multi-view sensing, generative model, diffusion model

I. INTRODUCTION

The sixth-generation (6G) wireless network will serve as a foundational service for various emerging applications, such as autonomous driving, extended reality (XR), intelligent robotics, etc [2]. These applications not only demand reliable wireless communication but also require the acquisition of environmental information. Integrated sensing and communication (ISAC) is a promising solution to address these requirements efficiently, aiming to reuse wireless communication systems to enable environment sensing functions, including detection, localization, and imaging [3]. Due to ISAC's efficiency in spectrum utilization and hardware resources, it has emerged as a focal point of current 6G research.

Part of this work was submitted to 2025 IEEE International Symposium on Personal, Indoor and Mobile Radio Communications (PIMRC) [1].

This work was supported in part by National Natural Science Foundation of China under Grants 62394292, Zhejiang Provincial Key R&D Program under Grant 2023C01021, and the Fundamental Research Funds for the Central Universities under Grant 226-2024-00069. (Corresponding author: Zhaoyang Zhang)

Z. Xing and Z. Zhang are with the College of Information Science and Electronic Engineering, Zhejiang University, Hangzhou 310027, China, also with the Institute of Fundamental and Transdisciplinary Research, Zhejiang University, Hangzhou 310058, China, and also with the Zhejiang Provincial Laboratory of Multi-Modal Communication Networks and Intelligent Information Processing, Hangzhou 310027, China (e-mail: ziqing_xing@zju.edu.cn; ning_ming@zju.edu.cn).

Z. Chen, H. Ruan and Z. Yang are with the College of Information Science and Electronic Engineering, Zhejiang University, Hangzhou 310027, China, and also with the Zhejiang Provincial Laboratory of Multi-Modal Communication Networks and Intelligent Information Processing, Hangzhou 310027, China (e-mail: ziruichen@zju.edu.cn; rhohenin@zju.edu.cn; yang_zhaohui@zju.edu.cn).

The fundamental issues in mono-static and bi-static ISAC scenarios have been widely studied, including beamforming strategy [4], hardware architecture [5], performance trade-off [6], etc. Building upon this foundation, some research efforts have explored emerging applications within these fundamental ISAC scenarios. For example, [7] leverages the initial access to achieve environment sensing and user localization, while [8] proposes an electromagnetic (EM) property sensing scheme for scatterers. However, the link between a single transceiver pair only captures partial environmental information, making it difficult to achieve high-quality sensing results from such a limited observation [9].

Given the limitations of single-link sensing, a series of studies [10]–[14] explored the use of multi-view observations formed by multiple base stations (BSs) and user equipments (UEs) in ISAC networks. This approach can alleviate the impact of occlusion and multiple scattering effect on wireless sensing problems, thereby enhancing the reconstruction of the shapes and EM properties of complex targets. However, existing multi-view sensing schemes are primarily based on traditional radar signal processing or compressed sensing algorithms, which typically perform inversion based on forward propagation models. Some of these methods also require approximate statistical models to characterize prior information of the target [15]. Consequently, the effectiveness of these traditional multi-view sensing methods highly depends on the accuracy of the modeling.

To overcome the reliance of traditional algorithms on statistical priors and explicit forward modeling, a number of research efforts have explored the application of artificial intelligence (AI) to address challenges in ISAC systems, such as hardware impairment compensation [16], intelligent beamforming [17], and high-precision parameter estimation [18]. Furthermore, [19] proposed a distributed aggregation scheme for multi-device sensing features to perform target classification. These advancements demonstrate the remarkable capability of AI in enabling efficient ISAC. In addition, environmental sensing is essentially an inverse problem based on the EM propagation laws, thus combining model-driven and data-driven approaches is a promising direction toward more fine-grained sensing. Currently, researchers have designed physics-informed neural networks to solve the EM inverse scattering problem, a fundamental physical problem in wireless imaging [20], [21]. However, these methods are not specifically tailored for wireless communication systems and cannot effectively handle diverse scenario configurations.

Different from classical AI techniques that build deterministic mappings, generative AI (GenAI) leverages probabilistic models to infer latent distributions from large-scale data, offering a more versatile way to discover fundamental mechanisms [22]. Recently, GenAI has inspired novel approaches for radio

frequency signal processing [23], channel representation [24], [25], and intelligent localization [26]. These advancements demonstrate GenAI's immense potential in uncovering the underlying physical laws of wireless data and performing rule-based generation for both signals and scenario characteristics, propelling a new path toward intelligent ISAC systems. Wang et al. outlined potential GenAI-enhanced ISAC physical layer technologies [27] and proposed a diffusion model-assisted human flow detection scheme as a case study [28]. Jiang et al. further employed a diffusion model for the target imaging task in a mono-static ISAC scenario [29]. However, these existing works mainly apply GenAI to partial processing stages of sensing algorithms and lack scalability for multi-BS multi-UE scenarios. These limitations constrain the effectiveness of GenAI in multi-device collaborative sensing systems.

To address these issues, this paper proposes a novel generative multi-view (Gen-MV) sensing framework, which fuses the channel state information (CSI) from multiple BSs and UEs to achieve EM imaging of the target within the region of interest (RoI). In response to variable view configurations in sensing scenarios, we introduce a general multi-view channel encoder for target feature extraction. Its main function is to eliminate target-irrelevant BS and UE positions from the CSI under different views, and fuse the multi-view channel features to integrate scene information. Subsequently, we employ a point cloud diffusion model with weighted loss to reconstruct the target shape and EM properties under the guidance of the extracted target features. The proposed Gen-MV sensing framework embeds physics-informed models into conditional generative learning, effectively handling dynamic changes in the positions and quantities of ISAC devices, and enhancing sensing quality with multi-view channels. The main contributions of this paper are summarized as follows:

- Based on the EM scattering channel model, we formulate the multi-view sensing problem using uplink CSI, explore the advantages of multi-view joint processing, and propose a Gen-MV sensing framework as a general solution. It mainly consists of a multi-view channel encoder and a target generator with conditioning mechanisms.
- In the multi-view channel encoder, we decouple the channel features from the positions of the BS and UE through a multiplicative positional embedding. Then, we implement three baseline encoders using classical architectures and further design an interleaved correlation learning architecture by leveraging the intrinsic physical structure of the multi-view channel.
- We represent the target using a shape-EM point cloud and employ a diffusion model to achieve generative target reconstruction. To address the distributional differences in the geometric shape and EM properties of the target, we propose a shape-EM weighted loss function to train the complete model.
- Through extensive numerical experiments, we demonstrate that the proposed schemes can flexibly accommodate variable positions and quantities of BSs and UEs, leveraging multi-view CSI to achieve effective target imaging. Ablation studies further validate the working mechanisms and design rationale of our solutions.

The remainder of this paper is organized as follows. Section

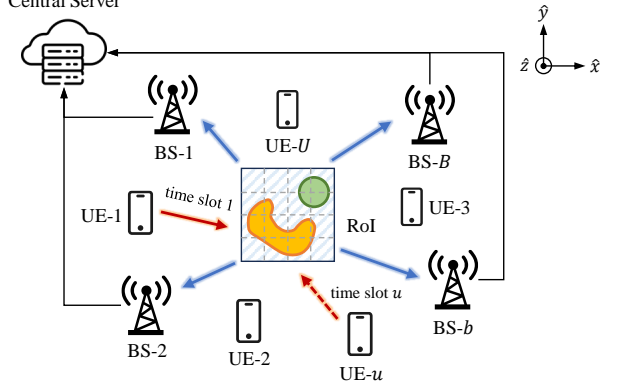


Fig. 1. The considered multi-view uplink sensing scenario.

II introduces the system model, including the scenario setup and EM channel modeling. In Section III, we propose the Gen-MV sensing framework, introduce the design of the multi-view channel encoder, and derive the target reconstruction process based on the diffusion model. Section IV provides performance evaluations and ablation studies of our proposed scheme. Finally, we conclude our work in Section V.

Notations: Fonts a , \mathbf{a} , and \mathbf{A} represent scalars, vectors, and matrices, respectively. $\mathbf{a}[m]$ and $\mathbf{A}[m, n]$ denote the m -th element of vector \mathbf{a} and the (m, n) -th element of matrix \mathbf{A} , respectively. $\text{vec}(\mathbf{A})$ denotes the vectorization of matrix \mathbf{A} and $\text{reshape}(\mathbf{a}, (M, N))$ denotes reshaping vector \mathbf{a} into an $M \times N$ matrix. \otimes denotes the Kronecker product and $*$ denotes the Khatri–Rao product. \odot , \oplus , and ∇ denote the Hadamard product, concatenation, and gradient operators, respectively. $D_{\text{KL}}(q(\mathbf{x}) \parallel p(\mathbf{x}))$ denotes the Kullback–Leibler (KL) divergence from distribution $q(\mathbf{x})$ to distribution $p(\mathbf{x})$. In physics, ϵ_0 , μ_0 , and c represent the permittivity, permeability, and speed of light in vacuum, respectively.

II. SYSTEM MODEL

A. Multi-View Wireless Sensing Scenario

We consider an uplink wireless sensing scenario as shown in Fig. 1. In this scenario, B BSs are deployed, each equipped with a uniform linear array (ULA) of N_r antennas, while U single-antenna UEs are actively transmitting. Each UE transmits pilot signals that are scattered by the target within the RoI and subsequently received by all BSs. Orthogonal frequency division multiplexing (OFDM) is employed for signal modulation, with pilots transmitted over N_c subcarriers. Based on these pilots, each BS estimates the uplink CSI between itself and the corresponding UE. We define a transceiver pair as a single view. All BSs upload the CSI between each BS and all UEs to a central server, where all single-view CSI is combined to form the multi-view CSI for the subsequent sensing task.

It is assumed that different UEs transmit pilots in separate time slots to avoid inter-user interference, and the positions of all BSs and UEs are known. The line-of-sight (LOS) path between the UE and BS does not constrain environmental information, but it can be obtained based on the positions of the UE and BS, and then removed from the channel response. For simplicity, we will omit this part in the following analysis.

B. Signal Propagation and Channel Model

For convenience of presentation, we consider the two-dimensional (2-D) case with transverse-magnetic (TM) wave, where the electric field is oriented along the \hat{z} -axis and can be simplified as a scalar. We first analyze the system at the n -th subcarrier frequency f_n and then extend to the multi-frequency case. Let $s_{u,n}$ denote the pilot signal transmitted by the u -th UE, and let \mathcal{R} denote the ROI. For each position $\mathbf{r} \in \mathcal{R}$, the incident field generated by the u -th UE located at \mathbf{p}_u^{UE} is

$$E_{u,n}^i(\mathbf{r}) = jk_n \eta \int g_n(\mathbf{r}, \mathbf{p}) \cdot \delta(\mathbf{p} - \mathbf{p}_u^{\text{UE}}) s_{u,n} d\mathbf{p}, \quad (1)$$

where $g_n(\mathbf{r}, \mathbf{r}') = \frac{j}{4} H_0^{(1)}(k_n \|\mathbf{r} - \mathbf{r}'\|)$ is the Green's function in the 2-D case and $H_0^{(1)}$ denotes the zeroth order of Hankel function of the first kind. $k_n = 2\pi f_n / c$ is the wave number and $\eta = \sqrt{\mu_0 / \epsilon_0}$ is the characteristic impedance of free space [30]. The sensing targets are scattering media with specific shapes and EM characteristics. These properties are manifested as spatial distributions of relative permittivity and conductivity within the ROI, which can be compactly characterized using the contrast defined as

$$\chi_n(\mathbf{r}) = (\epsilon_r(\mathbf{r}) - 1) + j \cdot \frac{\sigma(\mathbf{r})}{2\pi f_n \epsilon_0}, \quad \text{for } \mathbf{r} \in \mathcal{R}, \quad (2)$$

where $\epsilon_r(\mathbf{r})$ and $\sigma(\mathbf{r})$ are the relative permittivity and conductivity at position \mathbf{r} , respectively. The wave-target interaction satisfies the following Lippmann-Schwinger equation [31],

$$E_{u,n}^t(\mathbf{r}) = E_{u,n}^i(\mathbf{r}) + k_n^2 \int_{\mathcal{R}} g_n(\mathbf{r}, \mathbf{r}') \chi_n(\mathbf{r}') E_{u,n}^t(\mathbf{r}') d\mathbf{r}', \quad (3)$$

where $E_{u,n}^t(\mathbf{r})$ is the total electric field at position \mathbf{r} . The scattered signals received by the BSs originate from the re-radiation of induced currents in the target. For the r -th antenna of the b -th BS, the received scattered field is

$$E_{b,r,u,n}^s(\mathbf{p}_{b,r}^{\text{BS,RX}}) = k_n^2 \int_{\mathcal{R}} g_n(\mathbf{p}_{b,r}^{\text{BS,RX}}, \mathbf{r}') \chi_n(\mathbf{r}') E_{u,n}^t(\mathbf{r}') d\mathbf{r}', \quad (4)$$

where $\mathbf{p}_{b,r}^{\text{BS,RX}}$ denotes the position of the corresponding receiving antenna.

By uniformly discretizing the ROI into D pixels, we can get its pixelized representation $\mathbf{x} = [\epsilon_r; \sigma]$, where $\epsilon_r, \sigma \in \mathbb{R}^{D \times 1}$ are the relative permittivity and conductivity at each pixel position. \mathbf{x} is a dual-channel image that describes the target information in the ROI, and the discretized contrast image $\chi \in \mathbb{C}^{D \times 1}$ can be obtained according to (2). By applying the method of moments (MoM) based on (1)-(3), we can derive the discretized total electric field induced by the u -th UE as

$$\mathbf{e}_{u,n}^t = [\mathbf{I} - \mathbf{G}_n \text{diag}(\chi_n)]^{-1} \mathbf{h}_{u,n}^{\text{U-R}} s_{u,n}, \quad (5)$$

where $\mathbf{h}_{u,n}^{\text{U-R}} \in \mathbb{C}^{D \times 1}$ denotes the spatial channel from the UE to ROI pixels, and $\mathbf{G}_n \in \mathbb{C}^{D \times D}$ is the discretized Green's function matrix for inter-pixel interactions. According to (4), the pilot signal received by the b -th BS on N_r antennas is

$$\mathbf{y}_{b,u,n} = \mathbf{H}_{b,n}^{\text{R-B}} \text{diag}(\chi_n) \mathbf{e}_{u,n}^t + \mathbf{n} \quad (6)$$

$$= \mathbf{h}_{b,u,n} s_{u,n} + \mathbf{n}, \quad (7)$$

where $\mathbf{H}_{b,n}^{\text{R-B}} \in \mathbb{C}^{N_r \times D}$ denotes the spatial channel from ROI pixels to the BS, and \mathbf{n} is additive white Gaussian noise.

According to (5)-(7), the spatial channel between the u -th UE and b -th BS is given by

$$\mathbf{h}_{b,u,n} = \mathbf{H}_{b,n}^{\text{R-B}} \mathbf{X}_n \mathbf{h}_{u,n}^{\text{U-R}} = \left((\mathbf{h}_{u,n}^{\text{U-R}})^T \otimes \mathbf{H}_{b,n}^{\text{R-B}} \right) \text{vec}(\mathbf{X}_n). \quad (8)$$

where $\mathbf{X}_n = \text{diag}(\chi_n) [\mathbf{I} - \mathbf{G}_n \text{diag}(\chi_n)]^{-1}$ is the channel response induced by the target. By stacking N_c subcarriers, we can obtain the vectorized form of spatial-frequency channel under a single view,

$$\mathbf{h}_{b,u} = [\mathbf{h}_{b,u,1}; \dots; \mathbf{h}_{b,u,N_c}] = \left((\check{\mathbf{H}}_u^{\text{U-R}})^T * \check{\mathbf{H}}_b^{\text{R-B}} \right) \text{vec}(\mathbf{X}). \quad (9)$$

It consists of the following three components,

$$\check{\mathbf{H}}_u^{\text{U-R}} = \text{diag} \left(\mathbf{h}_{u,1}^{\text{U-R}}, \dots, \mathbf{h}_{u,N_c}^{\text{U-R}} \right) = f_{\mathbf{H}_{\text{U-R}}}(\mathbf{p}_u^{\text{UE}}), \quad (10)$$

$$\check{\mathbf{H}}_b^{\text{R-B}} = \text{diag} \left(\mathbf{H}_{b,1}^{\text{R-B}}, \dots, \mathbf{H}_{b,N_c}^{\text{R-B}} \right) = f_{\mathbf{H}_{\text{R-B}}}(\mathbf{p}_b^{\text{BS}}), \quad (11)$$

$$\mathbf{X} = [\mathbf{X}_1, \dots, \mathbf{X}_{N_c}] = f_{\mathbf{X}}(\mathbf{x}), \quad (12)$$

which are related to the UE position \mathbf{p}_u^{UE} , the BS position \mathbf{p}_b^{BS} , and the target property \mathbf{x} , respectively. The CSI matrix form of (9) can be expressed as

$$\mathbf{H}_{b,u} = \text{reshape}(\mathbf{h}_{b,u}, (N_r, N_c)) = f_{\mathbf{H}}(\mathbf{x}, \mathbf{p}_b^{\text{BS}}, \mathbf{p}_u^{\text{UE}}). \quad (13)$$

We integrate the CSI from multiple views and the corresponding BS and UE positions into a unified set,

$$\mathcal{H} = \{(\mathbf{H}_{b,u}, \mathbf{p}_b^{\text{BS}}, \mathbf{p}_u^{\text{UE}}) | b = 1, \dots, B; u = 1, \dots, U\}, \quad (14)$$

which forms the multi-view channel data.

III. CONDITIONAL GENERATIVE LEARNING FOR MULTI-VIEW WIRELESS SENSING

According to (13), the multi-view channels $\{\mathbf{H}_{b,u}\}$ share the same target property \mathbf{x} , which can be interpreted as projections of the identical target features from different BS/UE views. Therefore, joint processing of multi-view channel data can enhance target reconstruction. The objective of multi-view target reconstruction is to find the inverse mapping of (13), formulated as

$$\hat{\mathbf{x}} = g(\mathcal{H}), \quad (15)$$

which aims to recover the target properties from multi-view CSI and corresponding BS/UE positions. The inverse mapping g can be implemented as an iterative algorithm or a classical AI model with deterministic input and output. Alternatively, it can also be designed based on powerful and flexible generative models to facilitate the learning of intrinsic physical properties from the data distribution.

In this section, we first introduce the proposed Gen-MV sensing framework, followed by the detailed design of the multi-view channel encoder and the target reconstruction scheme based on the diffusion model.

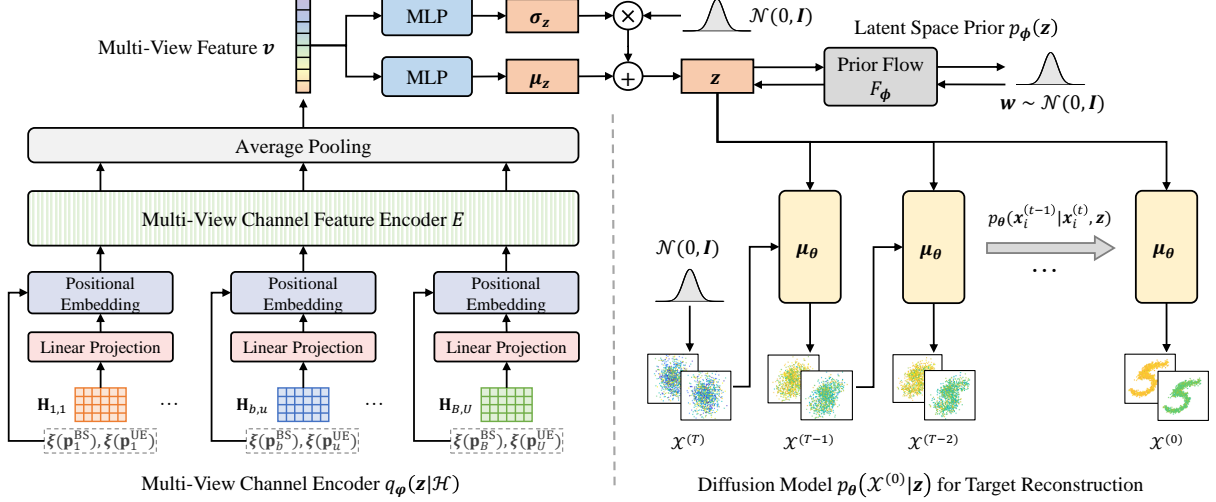


Fig. 2. The proposed Gen-MV sensing framework, which consists of a multi-view channel encoder $q_\varphi(z|\mathcal{H})$, a latent space prior $p_\phi(z)$, and a conditional generative model $p_\theta(x|z)$. Here, we employ a flow-based model F_ϕ to parameterize the prior $p_\phi(z)$, and implement a conditional point cloud diffusion model $p_\theta(x^{(0)}|z)$ for target reconstruction, where $x^{(0)}$ is the point cloud representation of the target properties x .

A. Gen-MV Sensing Framework

From the perspective of generative learning, we aim to model the conditional probability $p(x|\mathcal{H})$ based on measurement data. It enables us to perform the reconstruction process in (15) through maximum a posteriori (MAP) or minimum mean square error (MMSE) estimation. To achieve this, we can train a probabilistic model $p_\theta(x|\mathcal{H})$ with parameter θ to approximate the true distribution $p(x|\mathcal{H})$, where the training objective is to maximize the log-likelihood $\log p_\theta(x|\mathcal{H})$.

However, maximizing the posterior distribution is generally intractable. According to the conditional variational autoencoder (CVAE) proposed in [32], we introduce a latent variable z and a learnable distribution $q_\varphi(z|\mathcal{H}, x)$ to construct the evidence lower bound (ELBO) of $\log p_\theta(x|\mathcal{H})$, which is

$$\begin{aligned} \log p_\theta(x|\mathcal{H}) &= \log \left(\mathbb{E}_{q_\varphi(z|\mathcal{H}, x)} \left\{ \frac{p_\theta(x, z|\mathcal{H})}{q_\varphi(z|\mathcal{H}, x)} \right\} \right) \\ &\stackrel{(a)}{\geq} \mathbb{E}_{q_\varphi(z|\mathcal{H}, x)} \log \frac{p_\theta(x, z|\mathcal{H})}{q_\varphi(z|\mathcal{H}, x)} \\ &= \mathbb{E}_{q_\varphi(z|\mathcal{H}, x)} \left[\log p_\theta(x|z, \mathcal{H}) - \log \frac{q_\varphi(z|\mathcal{H}, x)}{p_\theta(z|\mathcal{H})} \right] \\ &\triangleq \text{ELBO}(x, \mathcal{H}), \end{aligned} \quad (16)$$

where (a) is due to Jensen's inequality. Therefore, we can implicitly optimize the log-likelihood $\log p_\theta(x|\mathcal{H})$ by minimizing the following loss function:

$$\begin{aligned} L_{\text{ELBO}}(x, \mathcal{H}) &\triangleq \mathbb{E}_{q_\varphi(z|\mathcal{H}, x)} [-\log p_\theta(x|z, \mathcal{H})] \\ &\quad + D_{\text{KL}}(q_\varphi(z|\mathcal{H}, x) \parallel p_\theta(z|\mathcal{H})). \end{aligned} \quad (17)$$

Although the above scheme is feasible for training a generative sensing model, we observe that it suffers from slow convergence and underperforming results in practice. A potential reason for this issue is the discrepancy between the training and inference objectives. Specifically, in the training stage, since x is provided as a condition in $q_\varphi(z|\mathcal{H}, x)$, the first term of (17) can reduce to compressing and reconstructing x using a variational autoencoder (VAE). This process is significantly easier than the inference task of reconstructing

x from \mathcal{H} based on $p_\theta(z|\mathcal{H})$ and $p_\theta(x|z, \mathcal{H})$. Although the KL divergence term in (17) encourages alignment between $q_\varphi(z|\mathcal{H}, x)$ and $p_\theta(z|\mathcal{H})$, this inconsistency still negatively impacts the model's performance. Our experiments indicate that relaxing (17) to the following training objective leads to a more concise and efficient model:

$$\begin{aligned} \tilde{L}_{\text{ELBO}}(x, \mathcal{H}) &\triangleq \mathbb{E}_{q_\varphi(z|\mathcal{H})} [-\log p_\theta(x|z)] \\ &\quad + D_{\text{KL}}(q_\varphi(z|\mathcal{H}) \parallel p_\phi(z)). \end{aligned} \quad (18)$$

According to (18), we decompose the Gen-MV sensing process into the following two steps:

- **Step 1:** A multi-view channel encoder $q_\varphi(z|\mathcal{H})$ extracts the target latent code z from the multi-view channel data \mathcal{H} . Inspired by VAE, we sample from a conditional distribution instead of using deterministic encoding and introduce a KL divergence term to align all posterior distributions with a common prior $p_\phi(z)$, ensuring a smooth and continuous latent space.
- **Step 2:** A conditional generative model $p_\theta(x|z)$ generates the target representation from the latent code z , thereby achieving the sensing of target properties.

The former focuses on effectively extracting target features from multi-view channels, while the latter can be implemented by integrating conditioning mechanisms into generative models. This approach decouples the design of the channel encoder and the target reconstruction process, providing a flexible Gen-MV sensing framework.

The schematic diagram of the overall framework is illustrated in Fig. 2. In the following subsections, we propose specific designs for the channel encoder and introduce a generative sensing scheme based on a diffusion model.

B. Multi-View Channel Encoder

As shown in (14), the channel from each view needs to be combined with the positions of the BS and UE to fully characterize the single-view observation. For each single-view CSI, we flatten it and pass it through a fully-connected layer

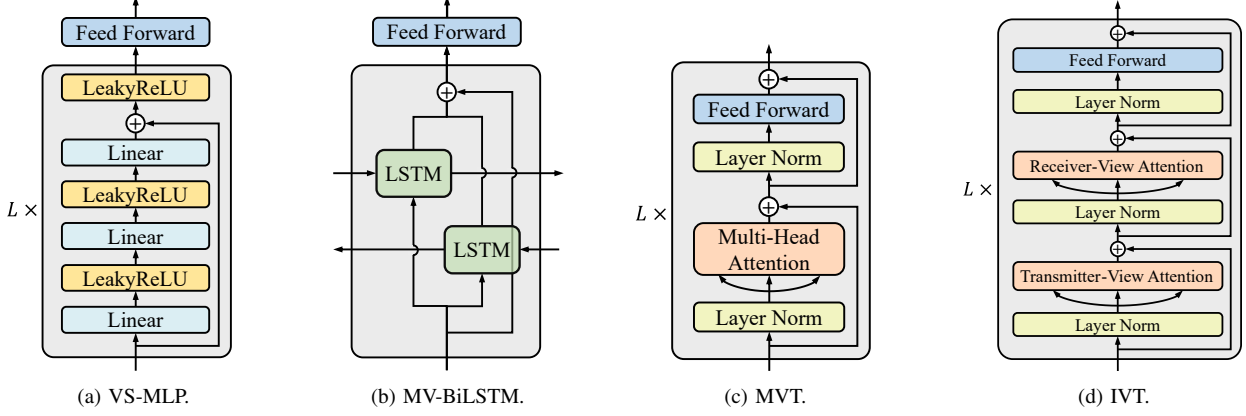


Fig. 3. Four structural designs for the multi-view channel feature encoder E . All feed-forward networks are two-layer MLPs with a hidden dimension of $2d_v$.

with parameters \mathbf{W}_h and \mathbf{b}_h to project it into a channel vector with dimension d_v ,

$$\mathbf{h}_{b,u} = \mathbf{W}_h \text{vec}(\mathbf{H}_{b,u}) + \mathbf{b}_h, \quad \forall b, u. \quad (19)$$

For the corresponding BS and UE positions, we first employ the positional encoding function in [33] to map spatial coordinates into higher dimensional vectors to capture the high-frequency variations of CSI in the space, i.e.

$$\begin{aligned} \boldsymbol{\xi}(\mathbf{p}) = [\mathbf{p}; \sin(2^0 \pi \mathbf{p}); \cos(2^0 \pi \mathbf{p}); \dots; \\ \sin(2^{d_p-1} \pi \mathbf{p}); \cos(2^{d_p-1} \pi \mathbf{p})], \end{aligned} \quad (20)$$

where \mathbf{p} is the spatial coordinate and d_p denotes the number of encoding frequencies. By concatenating the encoded BS and UE position vectors, we can get the view vector to denote the view position, formulated as

$$\boldsymbol{\xi}_{b,u} = \boldsymbol{\xi}(\mathbf{p}_b^{\text{BS}}) \oplus \boldsymbol{\xi}(\mathbf{p}_u^{\text{UE}}). \quad (21)$$

Embedding the view position into the channel vector is crucial and fundamentally different from the positional embedding in natural language processing (NLP). In natural language, the meaning of a word is relatively independent of its position in the text. Additionally, word embeddings and their positional encodings are inherently discrete and can be regarded as transformed representations of one-hot vectors. Due to the approximate orthogonality of random high-dimensional vectors, NLP commonly employs additive positional embeddings, enabling the model to separate lexical and positional information in later stages. In contrast, the wireless channel is highly correlated with its view position, and both are physical quantities with continuous values. These factors challenge the adaptability of additive positional embedding in wireless sensing models. According to (9), the channel $\mathbf{h}_{b,u}$ is formed by the coupling of $((\check{\mathbf{H}}_u^{\text{U}-\text{R}})^T * \check{\mathbf{H}}_b^{\text{R}-\text{B}})$ and \mathbf{X} through a linear transformation, where the two terms respectively contain the information of the view position and the target. Inspired by this, we construct a linear transformation to decouple the channel vector from the view position, formulated as

$$\mathbf{h}_{b,u}^{\text{in}} = \boldsymbol{\Gamma}(\boldsymbol{\xi}_{b,u}) \cdot \mathbf{h}_{b,u} = \boldsymbol{\gamma}(\boldsymbol{\xi}_{b,u}) \odot \mathbf{h}_{b,u}, \quad \forall b, u, \quad (22)$$

where $\boldsymbol{\Gamma}$ is a learnable transformation matrix derived from the view vector $\boldsymbol{\xi}_{b,u}$ and is assumed to be diagonal for easier model learning, which can be simplified to a multiplicative positional embedding. $\boldsymbol{\gamma}(\cdot)$ is a fully-connected layer with

input-output dimensions of $4 \cdot (2d_p + 1) \rightarrow d_v$, and $\{\mathbf{h}_{b,u}^{\text{in}}\}$ are channel vectors after positional embedding.

To achieve a comprehensive measurement of the scattered field for high-quality sensing, it is essential to fuse CSI from multiple views to obtain the target latent code \mathbf{z} . First, we extract features from the embedded channel vectors through a multi-view channel feature encoder E , which can be formulated generally as

$$\{\mathbf{h}_{b,u}^{\text{out}} \mid \forall b, u\} = E\left(\{\mathbf{h}_{b,u}^{\text{in}} \mid \forall b, u\}\right). \quad (23)$$

Through average pooling, the channel features from all views are aggregated into a multi-view feature vector \mathbf{v} ,

$$\mathbf{v} = \frac{1}{B \cdot U} \sum_{b,u} \mathbf{h}_{b,u}^{\text{out}}. \quad (24)$$

Finally, the posterior distribution of the target latent code \mathbf{z} is modeled as

$$\mathbf{z} \sim \mathcal{N}(\mathbf{z}; \boldsymbol{\mu}_z(\mathbf{v}), \text{diag}(\boldsymbol{\sigma}_z(\mathbf{v}))), \quad (25)$$

where $\boldsymbol{\mu}_z(\cdot)$ and $\boldsymbol{\sigma}_z(\cdot)$ are shallow multilayer perceptrons (MLPs) with input-output dimensions of $d_v \rightarrow d_z$, and the sampling of \mathbf{z} is performed via the reparameterization trick.

The complete multi-view channel encoder $q_\varphi(\mathbf{z}|\mathcal{H})$ is constructed by cascading (19)-(25), as shown in the left part of Fig. 2. With the multi-view channel feature encoder E serving as the core module, its design determines the effectiveness of multi-view fusion. Below, we implement the encoder E using three classical neural networks as baselines, and further propose an interleaved correlation learning architecture specifically designed for multi-view channel data.

1) *View-Shared MLP (VS-MLP)*: According to (13), all single-view channels share the identical propagation function $f_{\mathbf{H}}$ and target property \mathbf{x} . Leveraging this characteristic, a basic encoder E processes each single-view channel in parallel through a shared feature extractor, with multi-view information fusion entirely handled by subsequent average pooling. For single-view feature extraction, we utilize a MLP shown in Fig. 3(a), with its parameters shared across all views.

2) *Multi-View BiLSTM (MV-BiLSTM)*: Although VS-MLP is effective and parameter-efficient, average pooling is insufficient for fusing multi-view information. In [34], the authors achieved high-precision localization by accumulating channel features across multiple frequencies using Long Short Term

Memory (LSTM). Inspired by this, we process $\{\mathbf{h}_{b,u}^{\text{in}}\}$ as a sequence of length $B \times U$ and design a Bidirectional LSTM (BiLSTM) in Fig. 3(b) as the encoder E to integrate multi-view channel features. Compared to LSTM, BiLSTM introduces bidirectional feature accumulation, which enables each output feature to incorporate information from all views, enhancing compatibility with subsequent average pooling.

3) *Multi-View Transformer (MVT)*: As shown in (14), the multi-view channel data \mathcal{H} is an unordered set. However, MV-BiLSTM is a sequential model and cannot guarantee permutation invariance of the multi-view channel encoder. To address this, we designed the MVT, as illustrated in Fig. 3(c). MVT treats $\{\mathbf{h}_{b,u}^{\text{in}}\}$ as a set with $B \times U$ elements and computes pairwise correlations between channel vectors across all views through self-attention for feature extraction. It resolves the long-range dependency issue in LSTMs, and ensures permutation equivariance between input and output. With subsequent average pooling, the MVT-based multi-view channel encoder strictly satisfies permutation invariance.

4) *Interleaved-View Transformer (IVT)*: The three classical architectures mentioned above can all be utilized for multi-view channel feature encoding, and we implement them as baseline models. However, through deeper exploration of the inherent characteristics of multi-view channels, more efficient encoder designs can be achieved. By arranging all view's channels into the following partitioned matrix:

$$\mathbf{H}_{\text{mv}} = \begin{bmatrix} \mathbf{H}_{1,1} & \cdots & \mathbf{H}_{1,U} \\ \vdots & \ddots & \vdots \\ \mathbf{H}_{B,1} & \cdots & \mathbf{H}_{B,U} \end{bmatrix} \quad (26)$$

$$= \begin{bmatrix} f_{\mathbf{H}}(\mathbf{x}, \mathbf{p}_1^{\text{BS}}, \mathbf{p}_1^{\text{UE}}) & \cdots & f_{\mathbf{H}}(\mathbf{x}, \mathbf{p}_1^{\text{BS}}, \mathbf{p}_U^{\text{UE}}) \\ \vdots & \ddots & \vdots \\ f_{\mathbf{H}}(\mathbf{x}, \mathbf{p}_B^{\text{BS}}, \mathbf{p}_1^{\text{UE}}) & \cdots & f_{\mathbf{H}}(\mathbf{x}, \mathbf{p}_B^{\text{BS}}, \mathbf{p}_U^{\text{UE}}) \end{bmatrix}, \quad (27)$$

we can observe that each row block's U channels share the same BS view, reflected in the shared $\check{\mathbf{H}}_b^{\text{R-B}}$ component, while each column block's B channels share the same UE view, reflected in the shared $\check{\mathbf{H}}_u^{\text{U-R}}$ component. As shown in (9), the mutual coupling of $\check{\mathbf{H}}_b^{\text{R-B}}$, $\check{\mathbf{H}}_u^{\text{U-R}}$, and the target information \mathbf{X} ultimately forms the CSI. Leveraging this intrinsic structural property, we designed the IVT illustrated in Fig. 3(d). Each IVT layer operates through:

- Transmitter-View Attention (TVA): Computes channel feature correlations between different UE views, with this operation being shared across all BS views.
- Receiver-View Attention (RVA): Computes channel feature correlations between different BS views, with this operation being shared across all UE views.
- Feed-Forward Network (FFN): Performs feature transformation.

The input $\{\mathbf{h}_{b,u}^{\text{in}}\}$ is structured as a $B \times U \times d_v$ tensor \mathbf{h}_0 . For the ℓ -th IVT layer, the computation process is formulated as

$$\mathbf{h}_\ell[b, :, :] = \mathbf{h}_{\ell-1}[b, :, :] + \text{TVA}(\text{LN}(\mathbf{h}_{\ell-1}[b, :, :])), \quad \forall b, \quad (28)$$

$$\mathbf{h}_\ell[:, u, :] = \mathbf{h}_\ell[:, u, :] + \text{RVA}(\text{LN}(\mathbf{h}_\ell[:, u, :])), \quad \forall u, \quad (29)$$

$$\mathbf{h}_\ell[b, u, :] = \mathbf{h}_\ell[b, u, :] + \text{FFN}(\text{LN}(\mathbf{h}_\ell[b, u, :])), \quad \forall b, u, \quad (30)$$

where $\ell = 1, \dots, L$ and L is the number of IVT layers. TVA and RVA are self-attention blocks that extract correlations

along the second and first dimensions of $\mathbf{h}_{(\cdot)}$ respectively, and LN denotes layer normalization. Therefore, IVT guarantees permutation invariance between multiple BSs/UEs and incorporating physical properties of multi-view channels into its structural design.

5) *Computational Complexity*: The computational complexity of multi-view channel encoding mainly comes from the encoder E . We assume that the hidden layer dimensions of all models are equal to the channel vector dimension d_v , and use L to denote the number of model layers. Both VS-MLP and MV-BiLSTM have a computational complexity of $O(LBUd_v^2)$. The difference lies in that VS-MLP allows parallel processing across views, while MV-BiLSTM performs bidirectional sequential operations and is not parallelizable. The computational complexity of MVT is $O(L(B^2U^2d_v + BUd_v^2))$, and that of IVT is $O(L(BU^2d_v^2 + B^2Ud_v^2 + BUd_v^2))$. IVT exhibits certain advantages over MVT when dealing with a large number of views. Due to the attention mechanism, both MVT and IVT support parallel computation.

Overall, the aforementioned four encoders process the multi-view channel data \mathcal{H} as four distinct data structures: VS-MLP treats them as independent observations, MV-BiLSTM processes them as sequential data, MVT organizes them as an unordered set, and IVT models them as a 2D interleaved collection. In Section IV, we will compare the effectiveness of these four model structures in extracting multi-view features.

C. Diffusion Model for Target Reconstruction

Since the target latent code \mathbf{z} extracted by the multi-view channel encoder contains the complete properties of the target, it is feasible to generate the corresponding target representation using appropriate conditional generative models. Different from the pixel-based representation \mathbf{x} in forward modeling, in the reconstruction process, we represent the target as a 4-D point cloud containing M normalized shape-EM points, $\mathcal{X}^{(0)} = \{\mathbf{x}_i^{(0)} | i = 1, \dots, M\}$. Each point is defined as

$$\mathbf{x}_i^{(0)} = \left[\frac{x_i - \mu_x}{v_x}, \frac{y_i - \mu_y}{v_y}, \frac{\varepsilon_i - \mu_\varepsilon}{v_\varepsilon}, \frac{\sigma_i - \mu_\sigma}{v_\sigma} \right]^\top, \quad (31)$$

where x_i , y_i , ε_i , σ_i denote the \hat{x} -axis coordinate, \hat{y} -axis coordinate, relative permittivity and conductivity of the i -th point, respectively, while $\mu_{(\cdot)}$ and $v_{(\cdot)}$ respectively denote the mean and standard deviation of the corresponding dimensions.

Compared to the pixel-based target representation \mathbf{x} in Section II-B, the point cloud $\mathcal{X}^{(0)}$ offers the following advantages:

- **Low redundancy**: Due to the sparsity of target distribution in the ROI, \mathbf{x} contains numerous background pixels, whereas the point cloud $\mathcal{X}^{(0)}$ only needs to represent the target and omits background information, resulting in reduced redundancy.
- **Probabilistic characteristic**: The point cloud $\mathcal{X}^{(0)}$ emphasizes the holistic distribution of points, which can be modeled as M independent samples from a point distribution $q(\mathbf{x}_i^{(0)} | \mathbf{z})$. This intrinsic stochasticity makes the point cloud more suitable for probabilistic generative models in target reconstruction.

Moreover, using distinct target representations for forward modeling and inverse reconstruction requires models to learn

implicitly embedded physical knowledge from data. This strategy eliminates the dependence on explicit and precise forward modeling in the reconstruction process.

In this subsection, we adopt a conditional point cloud diffusion model $p_{\theta}(\mathcal{X}^{(0)}|\mathbf{z})$ proposed in [35] to generate the reconstructed target based on the target latent code \mathbf{z} , and derive the optimization procedure of the complete model based on the proposed Gen-MV sensing framework.

1) *Forward Diffusion Process*: The forward diffusion process gradually transforms the original point cloud distribution $q(\mathbf{x}_i^{(0)})$ into a noise distribution $q(\mathbf{x}_i^{(T)})$. It can be modeled as a Markov chain,

$$q(\mathbf{x}_i^{(1:T)}|\mathbf{x}_i^{(0)}) = \prod_{t=1}^T q(\mathbf{x}_i^{(t)}|\mathbf{x}_i^{(t-1)}), \quad (32)$$

and the transition probability is defined as

$$q(\mathbf{x}_i^{(t)}|\mathbf{x}_i^{(t-1)}) = \mathcal{N}(\mathbf{x}_i^{(t)}; \sqrt{1 - \beta_t} \mathbf{x}_i^{(t-1)}, \beta_t \mathbf{I}), \quad (33)$$

where $t = 1, \dots, T$, with T being the maximum timestep in the diffusion process. The predefined noise variance schedule β_1, \dots, β_T controls the rate of the diffusion. Defining $\alpha_t \triangleq 1 - \beta_t$, $\bar{\alpha}_t \triangleq \prod_{s=1}^t \alpha_s$, the sampling of $\mathbf{x}^{(t)}$ in the forward diffusion can be derived from (32) and (33) as

$$\mathbf{x}_i^{(t)} = \sqrt{\alpha_t} \mathbf{x}_i^{(0)} + \sqrt{1 - \alpha_t} \epsilon_i^{(t)}, \quad \epsilon_i^{(t)} \sim \mathcal{N}(\mathbf{0}, \mathbf{I}). \quad (34)$$

2) *Reverse Diffusion Process*: The generation process is the reverse of the forward diffusion process, aiming to gradually generate a target point cloud from the noise distribution conditioned on the target latent code \mathbf{z} .

According to Bayes' theorem, the reverse transition probability conditioned on $\mathbf{x}_i^{(0)}$ can be derived from (33) and (34) as

$$q(\mathbf{x}_i^{(t-1)}|\mathbf{x}_i^{(t)}, \mathbf{x}_i^{(0)}) = \mathcal{N}(\mathbf{x}_i^{(t-1)}; \tilde{\mu}_t(\mathbf{x}_i^{(t)}, \mathbf{x}_i^{(0)}), \tilde{\beta}_t \mathbf{I}), \quad (35)$$

with

$$\tilde{\mu}_t(\mathbf{x}_i^{(t)}, \mathbf{x}_i^{(0)}) = \frac{1}{\sqrt{\alpha_t}} \left(\mathbf{x}_i^{(t)} - \frac{1 - \alpha_t}{\sqrt{1 - \bar{\alpha}_t}} \epsilon_i^{(t)} \right), \quad (36)$$

$$\tilde{\beta}_t = \frac{1 - \bar{\alpha}_{t-1}}{1 - \bar{\alpha}_t} \beta_t, \quad (37)$$

where $\epsilon_i^{(t)} = (\mathbf{x}_i^{(t)} - \sqrt{\alpha_t} \mathbf{x}_i^{(0)}) / \sqrt{1 - \bar{\alpha}_t}$. However, the $q(\mathbf{x}_i^{(t-1)}|\mathbf{x}_i^{(t)}, \mathbf{z})$ we needed is still intractable. Therefore, we need to construct a learnable Markov chain conditioned on \mathbf{z} to implement the reverse diffusion process, where input points are sampled from the noise distribution $p(\mathbf{x}_i^{(T)})$ to approximate $q(\mathbf{x}_i^{(T)})$, i.e.

$$p_{\theta}(\mathbf{x}_i^{(0:T)}|\mathbf{z}) = p(\mathbf{x}_i^{(T)}) \prod_{t=1}^T p_{\theta}(\mathbf{x}_i^{(t-1)}|\mathbf{x}_i^{(t)}, \mathbf{z}), \quad (38)$$

and the reverse transition probability is modeled as a learnable Gaussian distribution,

$$p_{\theta}(\mathbf{x}_i^{(t-1)}|\mathbf{x}_i^{(t)}, \mathbf{z}) = \mathcal{N}(\mathbf{x}_i^{(t-1)}; \mu_{\theta}(\mathbf{x}_i^{(t)}, t, \mathbf{z}), \tilde{\beta}_t \mathbf{I}). \quad (39)$$

Similar to $\tilde{\mu}_t$ in (36), the predicted mean μ_{θ} is defined as

$$\mu_{\theta}(\mathbf{x}_i^{(t)}, t, \mathbf{z}) = \frac{1}{\sqrt{\alpha_t}} \left(\mathbf{x}_i^{(t)} - \frac{1 - \alpha_t}{\sqrt{1 - \bar{\alpha}_t}} \epsilon_{\theta}(\mathbf{x}_i^{(t)}, t, \mathbf{z}) \right), \quad (40)$$

where ϵ_{θ} is a learnable noise predictor with parameter θ , and we implement it with a variant of MLP, which consists of a series of `concat``squash` layers [36].

3) *Optimization of the Complete Model*: For a given target point cloud $\mathcal{X}^{(0)}$ and its latent code \mathbf{z} , the training objective of the point cloud diffusion model is to maximize the log-likelihood $\log p_{\theta}(\mathcal{X}^{(0)}|\mathbf{z})$. By introducing the point clouds $\mathcal{X}^{(1:T)}$ in the diffusion process, we can construct the ELBO of $\log p_{\theta}(\mathcal{X}^{(0)}|\mathbf{z})$ as

$$\log p_{\theta}(\mathcal{X}^{(0)}|\mathbf{z}) = \log \left[\mathbb{E}_{q(\mathcal{X}^{(1:T)}|\mathcal{X}^{(0)})} \frac{p_{\theta}(\mathcal{X}^{(0:T)}|\mathbf{z})}{q(\mathcal{X}^{(1:T)}|\mathcal{X}^{(0)})} \right] \quad (41)$$

$$\stackrel{(a)}{\geq} \mathbb{E}_{q(\mathcal{X}^{(1:T)}|\mathcal{X}^{(0)})} \log \left(\frac{p_{\theta}(\mathcal{X}^{(0:T)}|\mathbf{z})}{q(\mathcal{X}^{(1:T)}|\mathcal{X}^{(0)})} \right) \quad (42)$$

$$\stackrel{(b)}{=} \mathbb{E}_{q(\mathcal{X}^{(1:T)}|\mathcal{X}^{(0)})} \left[\sum_{i=1}^M \log \left(\frac{p_{\theta}(\mathbf{x}_i^{(0:T)}|\mathbf{z})}{q(\mathbf{x}_i^{(1:T)}|\mathbf{x}_i^{(0)})} \right) \right], \quad (43)$$

where (a) is due to Jensen's inequality, and (b) comes from the independence of the points $\{\mathbf{x}_i^{(t)}|i = 1, \dots, M\}$ that constitute the point cloud $\mathcal{X}^{(t)}$ in each timestep t .

The training objective of the complete model is to maximize $\mathbb{E}_{q_{\text{data}}(\mathcal{X}^{(0)}, \mathcal{H})} [\log p_{\theta}(\mathcal{X}^{(0)}|\mathcal{H})]$ on paired target point clouds and multi-view channel data $(\mathcal{X}^{(0)}, \mathcal{H})$, where q_{data} denotes their joint distribution in the dataset. According to the proposed Gen-MV sensing framework, we can derive the ELBO loss L_{ELBO} of the complete model as

$$\mathbb{E}_{q_{\text{data}}(\mathcal{X}^{(0)}, \mathcal{H})} \left[-\log p_{\theta}(\mathcal{X}^{(0)}|\mathcal{H}) \right] \quad (44)$$

$$\stackrel{(a)}{\approx} \mathbb{E}_{q_{\text{data}}(\mathcal{X}^{(0)}, \mathcal{H})} \left\{ \mathbb{E}_{q_{\varphi}(\mathbf{z}|\mathcal{H})} \left[-\log p_{\theta}(\mathcal{X}^{(0)}|\mathbf{z}) \right] + D_{\text{KL}}(q_{\varphi}(\mathbf{z}|\mathcal{H}) \parallel p_{\phi}(\mathbf{z})) \right\} \quad (45)$$

$$\stackrel{(b)}{\leq} \mathbb{E}_{(\mathcal{X}^{(0)}, \mathcal{H})} \left\{ \mathbb{E}_{\mathbf{z}, \mathcal{X}^{(1:T)}} \sum_{i=1}^M \log \left(\frac{q(\mathbf{x}_i^{(1:T)}|\mathbf{x}_i^{(0)})}{p_{\theta}(\mathbf{x}_i^{(0:T)}|\mathbf{z})} \right) + D_{\text{KL}}(q_{\varphi}(\mathbf{z}|\mathcal{H}) \parallel p_{\phi}(\mathbf{z})) \right\} \quad (46)$$

$$\triangleq L_{\text{ELBO}}, \quad (47)$$

where (a) comes from the simplified ELBO loss $\tilde{L}_{\text{ELBO}}(\mathbf{x}, \mathcal{H})$ of the conditional generative model proposed in (18) with \mathbf{x} replaced by $\mathcal{X}^{(0)}$, and (b) is obtained by substituting (43). By applying the Markov chain property of the diffusion process specified in (32) and (38) and utilizing Bayes' theorem, we can further simplify L_{ELBO} as

$$L_{\text{ELBO}} = \mathbb{E}_q \left[\sum_{i=1}^M \underbrace{D_{\text{KL}}(q(\mathbf{x}_i^{(T)}|\mathbf{x}_i^{(0)}) \parallel p(\mathbf{x}_i^{(T)}))}_{L_i^{(T)}} \right. \\ \left. + \sum_{t=2}^T \underbrace{D_{\text{KL}}(q(\mathbf{x}_i^{(t-1)}|\mathbf{x}_i^{(t)}, \mathbf{x}_i^{(0)}) \parallel p_{\theta}(\mathbf{x}_i^{(t-1)}|\mathbf{x}_i^{(t)}, \mathbf{z}))}_{L_i^{(t-1)}} \right. \\ \left. - \underbrace{\log p_{\theta}(\mathbf{x}_i^{(0)}|\mathbf{x}_i^{(1)}, \mathbf{z})}_{L_i^{(0)}} + \underbrace{D_{\text{KL}}(q_{\varphi}(\mathbf{z}|\mathcal{H}) \parallel p_{\phi}(\mathbf{z}))}_{L_z} \right], \quad (48)$$

where $L_i^{(T)}$ is the KL divergence between two deterministic Gaussian distributions and is independent of learnable parameters. $L_i^{(t-1)}$ can be derived from (35) and (39), which is

$$L_i^{(t-1)} = \frac{1}{2\tilde{\beta}_t} \left\| \tilde{\mu}_t(\mathbf{x}_i^{(t)}, \mathbf{x}_i^{(0)}) - \boldsymbol{\mu}_{\theta}(\mathbf{x}_i^{(t)}, t, \mathbf{z}) \right\|^2 \quad (49)$$

$$= \frac{\beta_t^2}{2\tilde{\beta}_t \cdot \alpha_t(1 - \bar{\alpha}_t)} \left\| \boldsymbol{\epsilon}_i^{(t)} - \boldsymbol{\epsilon}_{\theta}(\mathbf{x}_i^{(t)}, t, \mathbf{z}) \right\|^2. \quad (50)$$

$L_i^{(0)}$ can be transformed into the same form as $L_i^{(t-1)}$ and merged with it. L_z can be regarded as a regularization term that aligns all posterior $q_{\varphi}(\mathbf{z}|\mathcal{H})$ from the multi-view encoder to a unified prior $p_{\phi}(\mathbf{z})$, thereby improving the structural coherence and manifold smoothness of the latent space. Here, we employ a normalizing flow [37] parameterized by ϕ to model the prior distribution $p_{\phi}(\mathbf{z})$, which maps a standard Gaussian distribution $p_{\mathbf{w}}(\mathbf{w}) = \mathcal{N}(\mathbf{w}; \mathbf{0}, \mathbf{I})$ to a complex distribution $p_{\phi}(\mathbf{z})$ through a learnable bijective function F_{ϕ} . According to the properties of the flow model, L_z can be formulated as

$$L_z = D_{\text{KL}} \left(q_{\varphi}(\mathbf{z}|\mathcal{H}) \parallel p_{\mathbf{w}}(\mathbf{w}) \cdot \left| \det \frac{\partial F_{\phi}}{\partial \mathbf{w}} \right|^{-1} \right), \quad (51)$$

where $\mathbf{w} = F_{\phi}^{-1}(\mathbf{z})$ and F_{ϕ} is implemented by the affine coupling layers [38]. By randomly sampling timestep t and discarding the timestep-specific coefficients in (50), we can reformulate (48) as the following standard diffusion loss:

$$L_{\text{standard}} = \mathbb{E}_{(\mathcal{H}, \mathcal{X}^{(0)}), t, \mathbf{z}, \boldsymbol{\epsilon}_i} \left\{ \frac{1}{4M} \times \sum_{i=1}^M \left\| \boldsymbol{\epsilon}_i - \boldsymbol{\epsilon}_{\theta}(\mathbf{x}_i^{(t)}, t, \mathbf{z}) \right\|^2 + \gamma_z \cdot L_z \right\}, \quad (52)$$

where averaging is performed over the quantity and dimensionality of points, and a coefficient γ_z is introduced to adjust the weight of L_z term.

In most scenarios, the spatial distribution complexity of targets typically differs between their geometric shape and EM material properties, leading to imbalanced reconstruction challenges associated with these two physical attributes. To further enhance reconstruction quality, we introduce the following shape-EM weighted diffusion loss:

$$L_{\text{shape-EM}} = \mathbb{E}_{(\mathcal{H}, \mathcal{X}^{(0)}), t, \mathbf{z}, \boldsymbol{\epsilon}_i} \left\{ \frac{1}{M} \times \sum_{i=1}^M (\gamma_s \cdot L_{s,i} + \gamma_{\text{EM}} \cdot L_{\text{EM},i}) + \gamma_z \cdot L_z \right\}, \quad (53)$$

where $L_{s,i} = \left\| \boldsymbol{\epsilon}_{i,s} - \boldsymbol{\epsilon}_{\theta,s}(\mathbf{x}_i^{(t)}, t, \mathbf{z}) \right\|^2$ and $L_{\text{EM},i} = \left\| \boldsymbol{\epsilon}_{i,\text{EM}} - \boldsymbol{\epsilon}_{\theta,\text{EM}}(\mathbf{x}_i^{(t)}, t, \mathbf{z}) \right\|^2$ respectively denote the diffusion loss for the i -th point in shape and EM dimensions, with subscripts s and EM representing the corresponding vector dimensions (i.e. dimensions 1-2 for shape and 3-4 for EM properties).

In the inference stage, we can perform iterative sampling based on (38)-(40) to generate target point clouds from noise samples. The training and inference procedures for the proposed Gen-MV sensing scheme are summarized in Algorithms 1 and 2.

Algorithm 1 Training of the Proposed Gen-MV Sensing

```

1: repeat
2:   Sample multi-view channel data and the corresponding
   target point cloud  $(\mathcal{H}, \mathcal{X}^{(0)})$  from the training set.
3:   Sample target latent code  $\mathbf{z} \sim q_{\varphi}(\mathbf{z}|\mathcal{H})$  through the
   multi-view channel encoder  $\varphi$ .
4:   Sample  $t \sim \text{Uniform}(\{1, \dots, T\})$ .
5:   for  $i = 1$  to  $M$  in parallel do
6:     Sample  $\boldsymbol{\epsilon}_i \sim \mathcal{N}(\mathbf{0}, \mathbf{I})$ .
7:      $\mathbf{x}_i^{(t)} = \sqrt{\bar{\alpha}_t} \mathbf{x}_i^{(0)} + \sqrt{1 - \bar{\alpha}_t} \boldsymbol{\epsilon}_i$ .
8:      $L_{s,i} = \left\| \boldsymbol{\epsilon}_{i,s} - \boldsymbol{\epsilon}_{\theta,s}(\mathbf{x}_i^{(t)}, t, \mathbf{z}) \right\|^2$ .
9:      $L_{\text{EM},i} = \left\| \boldsymbol{\epsilon}_{i,\text{EM}} - \boldsymbol{\epsilon}_{\theta,\text{EM}}(\mathbf{x}_i^{(t)}, t, \mathbf{z}) \right\|^2$ .
10:    end for
11:     $L_z = D_{\text{KL}}(q_{\varphi}(\mathbf{z}|\mathcal{H}) \parallel p_{\mathbf{w}}(F_{\phi}^{-1}(\mathbf{z})) \cdot \left| \det \frac{\partial F_{\phi}}{\partial \mathbf{w}} \right|^{-1})$ .
12:    Take gradient descent step on
    $\nabla_{\varphi, \phi, \theta} \frac{1}{M} \sum_{i=1}^M (\gamma_s \cdot L_{s,i} + \gamma_{\text{EM}} \cdot L_{\text{EM},i}) + \gamma_z \cdot L_z$ 
13: until converged

```

Algorithm 2 Inference of the Proposed Gen-MV Sensing

Input: Multi-view channel data \mathcal{H} , including each view's CSI and BS/UE positions.

Output: Reconstructed target point cloud $\hat{\mathcal{X}}^{(0)}$.

```

1: Sample target latent code  $\mathbf{z} \sim q_{\varphi}(\mathbf{z}|\mathcal{H})$  through the multi-
   view channel encoder  $\varphi$ .
2: for  $i = 1$  to  $M$  in parallel do
3:   Sample  $\hat{\mathbf{x}}_i^{(T)} \sim \mathcal{N}(\mathbf{0}, \mathbf{I})$ .
4:   for  $t = T$  to 1 do
5:      $\hat{\boldsymbol{\epsilon}}_i^{(t)} = \boldsymbol{\epsilon}_{\theta}(\hat{\mathbf{x}}_i^{(t)}, t, \mathbf{z})$ .
6:     Sample  $\boldsymbol{\epsilon} \sim \mathcal{N}(\mathbf{0}, \mathbf{I})$ .
7:      $\hat{\mathbf{x}}_i^{(t-1)} = \frac{1}{\sqrt{\alpha_t}} \left( \hat{\mathbf{x}}_i^{(t)} - \frac{1 - \alpha_t}{\sqrt{1 - \alpha_t}} \hat{\boldsymbol{\epsilon}}_i^{(t)} \right) + \tilde{\beta}_t \cdot \boldsymbol{\epsilon}$ .
8:   end for
9: end for
10:  $\hat{\mathcal{X}}^{(0)} = \{\hat{\mathbf{x}}_i^{(0)} | i = 1, \dots, M\}$ .

```

IV. NUMERICAL RESULTS

In this section, we evaluate the performance of the proposed Gen-MV sensing scheme. First, we introduce the experimental parameter settings and define the performance evaluation metric. Then, we present a variety of experimental results to comprehensively evaluate the models' sensing performance. Finally, we conduct ablation studies to validate the effectiveness of the positional embedding and the shape-EM weighted diffusion loss in our proposed scheme.

A. Experiment Settings

In this work, we set the RoI as a 2-D square region centered at $(0, 0)$ with dimensions $0.5\text{m} \times 0.5\text{m}$. The system operates at a central frequency $f_c = 3\text{GHz}$, and we use $N_c = 8$ subcarriers to transmit pilots with a subcarrier spacing of $\Delta f = 100\text{kHz}$. The BSs are deployed within a range of 80m to 100m from the origin, each equipped with $N_r = 4$ antennas in a ULA configuration, with the array normal pointing toward the origin. The total number of BSs $B \leq 16$. The UEs are randomly distributed within a range of 4m to 10m from the origin, with the number of UEs $U \leq 32$. In practice, this can refer to snapshots of several UEs moving within this area. We

synthesize homogeneous targets based on the MNIST dataset [39], assigning each target a relative permittivity $\varepsilon_r \in [1.5, 2.5]$ and a conductivity $\sigma \in [0, 0.1]$ (S/m). The scattering channel is simulated using the MoM, as described in Section II-B. We randomly generate 50,000 data samples, which are divided into training, validation, and test sets in an 8:1:1 ratio.

To analyze the capability of different network architectures in extracting multi-view features for wireless sensing, we construct the multi-view channel encoders using four different structures proposed in Section III-B for experimental comparison. Among them, VS-MLP, MVT, and IVT consist of 6 network layers, while MV-BiLSTM employs 3 layers of LSTM in each direction. Other model parameters remain consistent, with configurations detailed in Table I. The weighting coefficients in the loss function (53) are set as $\gamma_s = 0.45$, $\gamma_{EM} = 0.05$, and $\gamma_z = 1 \times 10^{-4}$. Under the settings of $B = 16$ and $U = 32$, the number of parameters and floating-point operations (FLOPs) of the four multi-view channel encoders are summarized in Table II. During training, we set the batch size to 128, the initial learning rate to 10^{-4} , and decay the learning rate by a factor of 0.8 every 10^5 steps. The total training process takes 10^6 steps, and the Adam optimizer is used for optimization.

TABLE I: Model parameter settings

Parameters	Value
Number of encoding frequencies d_p	10
Channel feature dimension d_v	256
Target latent code dimension d_z	128
Number of points M in the point cloud	1000
Maximum diffusion timestep T	100
Variance schedule $\{\beta_t\}$	$\beta_1 = 1 \times 10^{-4}$, linearly increasing to $\beta_T = 0.02$.

TABLE II: Parameter counts and FLOPs of four multi-view channel encoder architectures

Model	Parameter Counts	FLOPs
VS-MLP	1.59 Million	1.52 Giga
MV-BiLSTM	4.87 Million	4.88 Giga
MVT	3.30 Million	4.91 Giga
IVT	4.88 Million	5.06 Giga

To comprehensively evaluate the models' reconstruction performance in both shape and EM properties, we adopt the log-scale Chamfer Distance (log-CD) to evaluate target point cloud reconstruction quality, defined as

$$\text{log-CD (dB)} = 10 \log_{10} \left(\frac{1}{M} \sum_{\mathbf{x} \in \mathcal{X}} \min_{\hat{\mathbf{x}} \in \hat{\mathcal{X}}} \|\mathbf{x} - \hat{\mathbf{x}}\|_2^2 + \frac{1}{M} \sum_{\hat{\mathbf{x}} \in \hat{\mathcal{X}}} \min_{\mathbf{x} \in \mathcal{X}} \|\hat{\mathbf{x}} - \mathbf{x}\|_2^2 \right), \quad (54)$$

where \mathcal{X} is the point cloud sampled from the ground truth target and $\hat{\mathcal{X}}$ is the corresponding reconstruction result, and the logarithmic operation is applied to enhance the metric's sensitivity to small numerical differences. All evaluations are performed on dimensionless normalized shape-EM point clouds as defined in (31). Unless otherwise specified, the default number of views is set to $B = 16$ and $U = 32$ in performance evaluations to assess the performance limits of the models.

B. Performance Evaluation

1) *Generative Reconstruction Process*: Fig. 4 visualizes the generative reconstruction process of the conditional point cloud diffusion model for a target from the test set, where an IVT-based encoder is implemented to process multi-view channel data \mathcal{H} . As proposed in our scheme, the target latent code \mathbf{z} , which is extracted from \mathcal{H} by the multi-view channel encoder, guides the diffusion model to progressively generate high-quality target point clouds from random noise distributions, including clear geometric shapes and accurate EM property estimations.

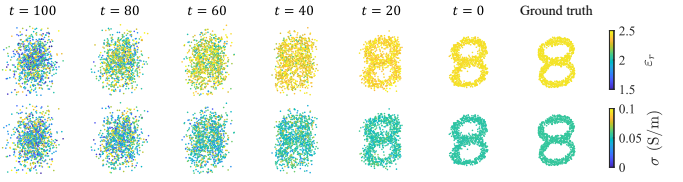


Fig. 4. Generative reconstruction process of a target based on the conditional point cloud diffusion model, where the multi-view channel encoder is implemented with IVT structure.

2) *Performance of Different Multi-View Channel Encoder Architectures*: According to our proposed Gen-MV sensing framework, the structural design of the multi-view channel encoder determines the effectiveness of extracting target features from multi-view CSI, thereby affecting the quality of subsequent reconstruction. Fig. 5 demonstrates several reconstructed targets of four multi-view encoder architectures, which are VS-MLP, MV-BiLSTM, MVT, and IVT. It can be observed that all encoder structures function properly and produce recognizable reconstruction results, demonstrating the broad applicability of our proposed Gen-MV sensing framework. In terms of details, VS-MLP produces relatively blurry reconstructed targets due to its lack of delicate multi-view feature interaction. MV-BiLSTM improves the reconstruction quality for the majority of samples, but it is still underperforming for several samples (e.g., the digit 5 in Fig. 5). MVT and IVT yield clearer reconstruction results, with IVT demonstrating superior performance in shape details and EM property accuracy for certain targets.

To comprehensively compare the capabilities of these four model architectures in extracting multi-view features of targets, Fig. 6 presents their cumulative distribution functions (CDFs) of the log-CD metric on the test set. Compared to VS-MLP, which processes each view independently, MV-BiLSTM and MVT introduce accumulative learning and correlation learning across multiple views, respectively, significantly boosting the model's sensing performance, which indicates the importance of multi-view fusion in wireless sensing. Among them, MVT utilizes the self-attention mechanism to address long-range dependencies while aligning with the permutation invariance of multi-view data, thereby achieving better performance than MV-BiLSTM. Unlike these three baseline models with classical structures, our proposed IVT introduces an innovative architecture with interleaved transmitter-receiver view attention. By leveraging the intrinsic structural properties of multi-view channels, this design incorporates more fine-grained physical information. As a result, IVT demonstrates superior multi-view channel feature extraction capabilities

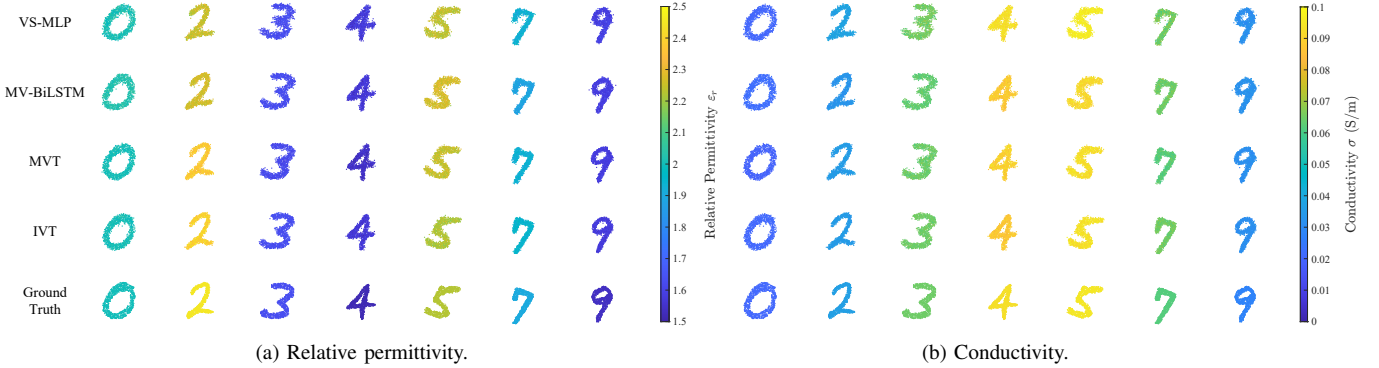


Fig. 5. Reconstruction results of several targets using four multi-view channel encoder architectures (i.e. VS-MLP, MV-BiLSTM, MVT, and IVT). The relative permittivity ϵ_r and conductivity σ at each point position are visualized by color mapping.

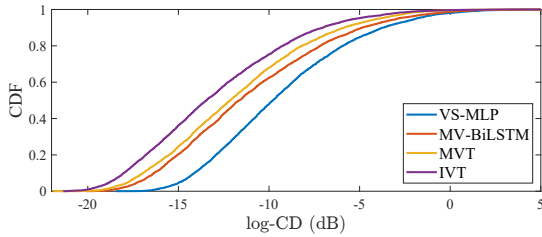


Fig. 6. CDFs of log-CD on the test set for four multi-view channel encoder architectures.

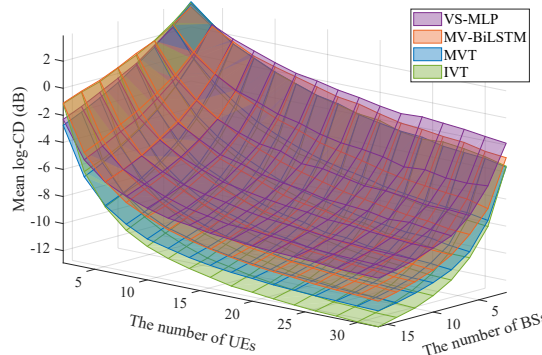


Fig. 7. Mean log-CD of reconstruction results for four multi-view channel encoder architectures across different numbers of BSs and UEs.

compared to other encoders, attaining both a higher sensing performance limit and better results on hard samples.

3) *Performance under Different Numbers of Views:* To analyze the importance of leveraging multi-view channel measurements in wireless sensing and evaluate the capability of different model architectures in processing multi-view data, Fig. 7 shows the mean log-CD of reconstruction results for four encoder architectures under variable numbers of BSs and UEs, and Table III lists the mean log-CD metric of these four encoders under three different numbers of views. It can be observed that all four models can operate effectively with variable BS/UE configurations, and the reconstruction quality is positively correlated with the number of views. It demonstrates that the proposed Gen-MV sensing framework can handle flexible BS/UE quantities and positions, effectively extracting target features from multi-view CSI to accomplish sensing tasks. Although multiple views are beneficial for obtaining comprehensive observations of targets, the improvement in reconstruction quality gradually diminishes as the number of views increases. This reflects the marginal effect of enhancing

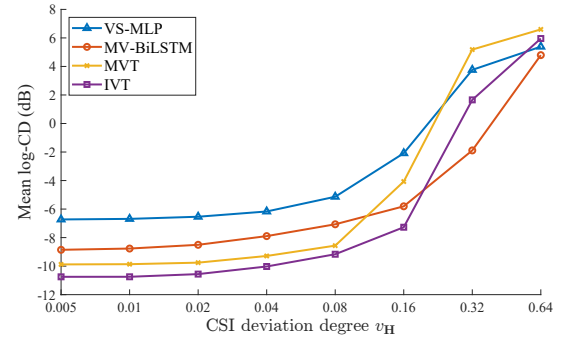


Fig. 8. Robustness evaluation of four multi-view channel encoder architectures.

TABLE III: Mean log-CD (dB) of four multi-view channel encoder architectures under different view configurations. The number of views N_{view} is represented as (number of BSs, number of UEs).

model \ N_{view}	(4, 8)	(8, 16)	(16, 32)
VS-MLP	-1.37	-6.25	-9.30
MV-BiLSTM	-1.48	-7.14	-11.01
MVT	-2.35	-8.57	-11.72
IVT	-2.78	-9.16	-12.90

sensing accuracy solely by increasing the number of views.

By comparing the reconstruction performance of the four encoder architectures in Fig. 7, we observe that when the number of views is sufficient, the reconstruction quality on the test set improves progressively from VS-MLP to MV-BiLSTM, MVT, and IVT. This suggests that incorporating more designs tailored to the structural and physical properties of multi-view data into the channel encoder can effectively enhance its feature extraction capabilities. As shown in Table III, IVT's performance with 8 UEs and 16 BSs approaches that of VS-MLP with 16 BSs and 32 UEs, which highlights the critical role of multi-view feature extraction architectures for generative multi-view wireless sensing.

4) *Robustness against Channel Disturbance:* To evaluate the impact of non-ideal channel estimation, we introduce a CSI disturbance modeled as $\tilde{\mathbf{H}}_{b,u} = \mathbf{H}_{b,u} \odot \mathbf{D}$, following [25], [34]. The elements of \mathbf{D} follow an independent and identically distributed (i.i.d.) Gaussian distribution $\mathcal{N}(1, v_{\mathbf{H}}^2)$, where $v_{\mathbf{H}}$ simulates the deviation degree of the lossy channel from the ideal channel. During training, $v_{\mathbf{H}}$ is randomly selected from the range [0.01, 0.08]. The relationship between testing performance and deviation degree is illustrated in

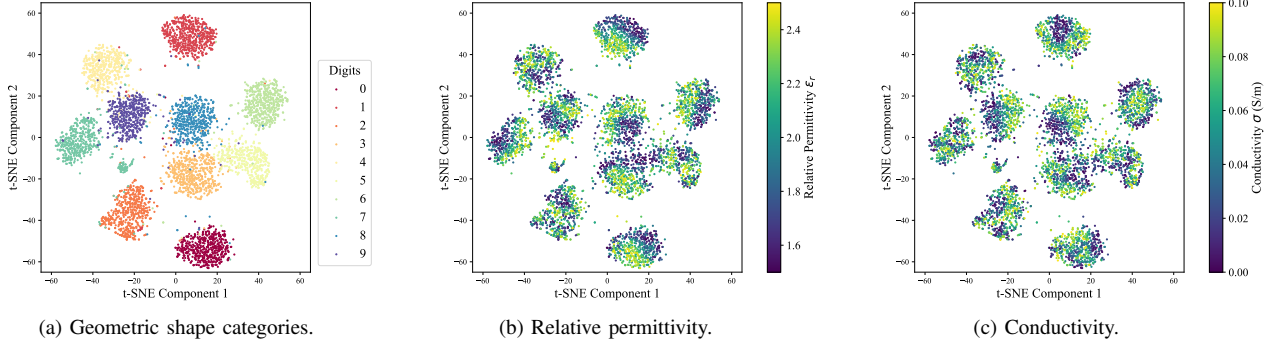


Fig. 9. t-SNE visualization of the latent space learned from the MNIST target dataset, where the multi-view channel encoder is implemented using IVT.

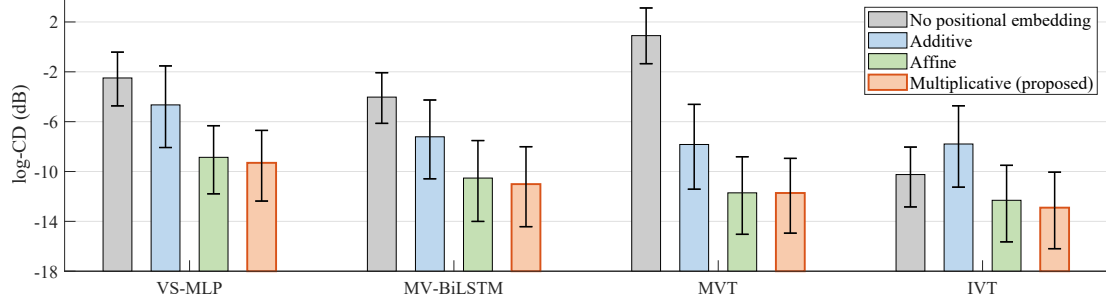


Fig. 10. Performance of four multi-view channel encoders under different positional embedding schemes, where the quartiles Q1 and Q3 are marked.

Fig. 8. Within the preset deviation range, all models exhibit stable sensing performance, indicating the proposed scheme's applicability to non-ideal CSI. Moreover, the attention-based MVT and IVT demonstrate better sensing accuracy under low deviation ($v_H \leq 0.08$), but they are more sensitive to increased deviation, showing significant performance degradation when $v_H > 0.16$. This is because the attention mechanism captures more fine-grained channel features, thereby achieving a higher upper bound of sensing accuracy, but it also makes models more susceptible to disturbances in CSI. Similar phenomena have also been reported in deep learning-based channel prediction and estimation tasks [25]. The robustness of the models can be further enhanced by tuning the preset deviation range, albeit with a reduction in upper-bound performance.

5) *Latent Space Representation of Target Features*: To analyze the distribution of latent representations of target features, we project the target latent code z generated by the multi-view channel encoder with IVT structure into a two-dimensional space using t-distributed stochastic neighbor embedding (t-SNE) [40]. The visualization results of geometric shape categories, relative permittivity, and conductivity are shown in Fig. 9. Due to the variational inference process of the Gen-MV framework and the constraints from the latent space prior model, the low-dimensional projections of the target latent codes exhibit clustering characteristics according to the geometric shape, with significant margins between most shape categories. Within each cluster, the EM properties, including relative permittivity and conductivity, also exhibit smooth and regular distributions. These phenomena reflect the structure and semantic information of the target latent space, which further indicates that our proposed channel encoder can effectively extract shape and EM property information of targets from multi-view channels, suggesting its potential applications for target classification and material detection.

C. Ablation Studies

1) *Ablation Study on Positional Embedding*: To validate the effectiveness of the proposed multiplicative positional embedding in processing channel data, we designed the following three comparative schemes: (i) No embedding of BS/UE positional information; (ii) Classical additive positional embedding, i.e., modifying (22) to $h_{b,u}^{\text{in}} = h_{b,u} + \beta(\xi_{b,u})$; (iii) Affine-type positional embedding, i.e., modifying (22) to $h_{b,u}^{\text{in}} = \gamma(\xi_{b,u}) \odot h_{b,u} + \beta(\xi_{b,u})$, where β and γ are fully connected layers. Fig. 10 illustrates the reconstruction performance of each encoder architecture under the four positional embedding schemes, with the first (Q1) and third (Q3) quartiles marked. Compared to the additive positional embedding in NLP, multiplicative positional embedding significantly enhances model performance, and this conclusion holds for all proposed multi-view channel encoder architectures. Furthermore, employing affine-type positional embedding (a combination of multiplicative and additive approaches) shows no performance gain over multiplicative embedding. These experimental results demonstrate the effectiveness and universality of the multiplicative operation in embedding BS/UE positions into channel features.

Additionally, we notice that for the three baseline encoders, the absence of positional embedding renders the models nearly inoperative, but IVT still operates effectively under such conditions. This is because IVT introduces the physical properties of multi-view channels as a structural prior for the network, enabling it to extract environmental features by leveraging the spatial correspondence of transmitters and receivers across multiple views — even in the absence of exact BS/UE locations. Moreover, for IVT, explicitly embedding the view positions via the multiplicative operation remains more effective, whereas improper additive embedding can disrupt the model and degrade performance. These results further

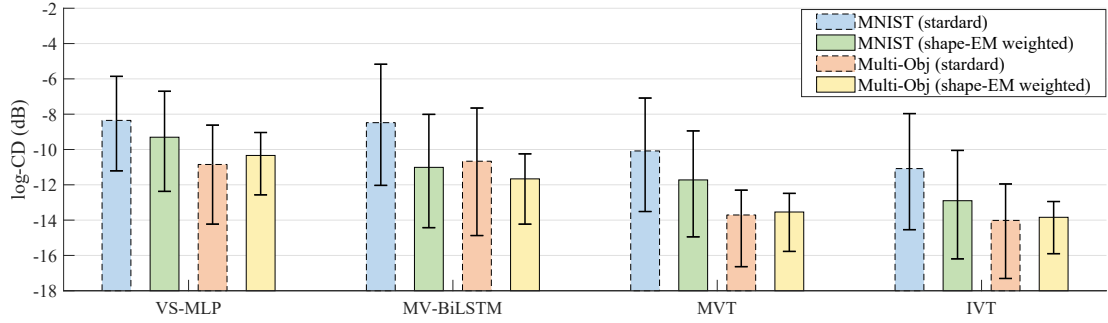


Fig. 11. Performance of four multi-view channel encoders on the MNIST and Multi-Obj datasets, with standard ($\gamma_s = \gamma_{EM} = 0.25$) and shape-EM weighted ($\gamma_s = 0.45, \gamma_{EM} = 0.05$) diffusion loss, where the quartiles Q1 and Q3 are marked.

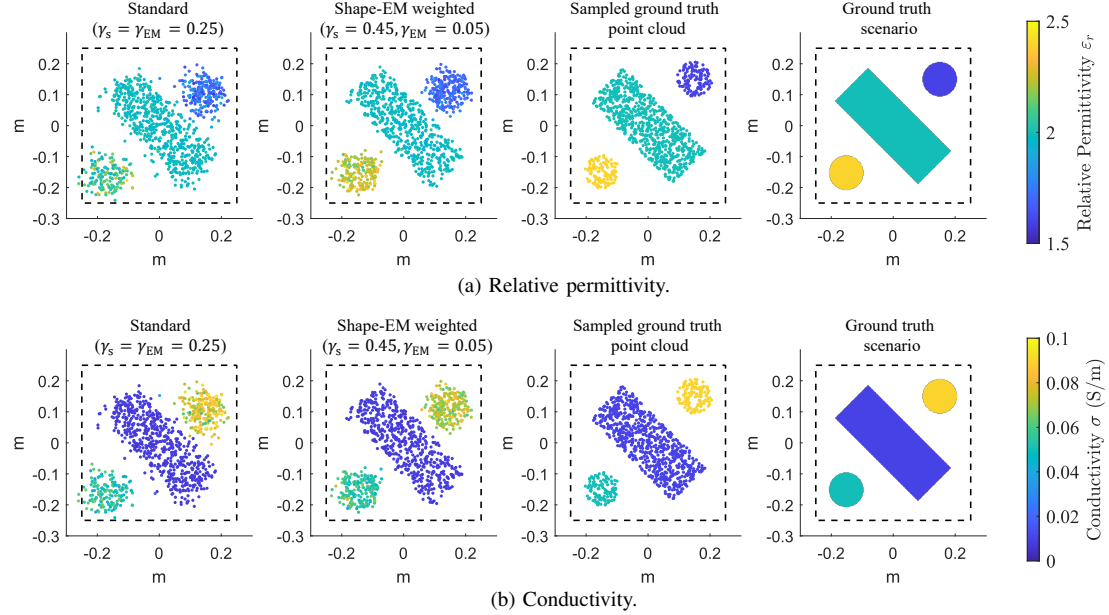


Fig. 12. Reconstruction results of IVT-based models using different loss weighting schemes on a hard sample from the Multi-Obj dataset. The ROI is marked with a dashed box.

indicate that incorporating appropriate physical priors into the Gen-MV sensing model enhances its capability to extract environmental features.

2) *Ablation Study on Shape-EM Weighted Diffusion Loss:* To validate the effectiveness of the proposed shape-EM weighted diffusion loss in improving reconstruction quality, we conduct experiments on the MNIST target dataset using the standard diffusion loss¹ and the shape-EM weighted diffusion loss with coefficients $\gamma_s = 0.45, \gamma_{EM} = 0.05$. To further evaluate the proposed method for multi-object imaging, we refer to [20], [21] and construct a heterogeneous multi-target dataset, *Multi-Obj*, to conduct the same ablation study, where several cuboids and cylinders are randomly placed within the ROI. The relative permittivity ϵ_r of each object is sampled from [1.5, 2.5], and the conductivity σ from [0, 0.1] (S/m). The evaluation results are presented in Fig. 11.

For the MNIST dataset, where the EM properties of the target in each scene are homogeneous, shape reconstruction is the main challenge. In this case, applying shape-EM weighted loss significantly improves overall reconstruction performance. In contrast, for the Multi-Obj dataset, the models have to

estimate the position, shape, and EM properties of multiple targets simultaneously. Since the EM property distribution becomes complicated, placing more emphasis on shape reconstruction does not yield a clear improvement in average log-CD performance. However, according to error bars, the weighted scheme provides more consistent reconstruction performance across the dataset and performs better on hard samples compared to the standard diffusion loss. To provide an intuitive illustration, Fig. 12 shows the reconstruction results for a hard sample with compactly distributed objects in the Multi-Obj dataset, obtained from the models trained with these two loss weighting schemes, where an IVT-based multi-view channel encoder is used. It can be observed that even under heterogeneous multi-object conditions, assigning more weight to the shape component in the loss function still helps recover clearer object contours, which is beneficial for multi-object segmentation and localization. Therefore, the shape-EM weighted diffusion loss provides a flexible trade-off for joint shape and EM property sensing, and emphasizing shape reconstruction is practical in a wide range of scenarios.

¹Evidently, the standard diffusion loss is equivalent to using a shape-EM weighted diffusion loss with $\gamma_s = \gamma_{EM} = 0.25$.

V. CONCLUSIONS

In this paper, we propose a novel conditional generative learning framework for multi-view wireless sensing, leveraging uplink CSI from multiple BSs and UEs in ISAC networks to achieve high-quality reconstruction of the target within the RoI. Overall, we develop an end-to-end sensing model by integrating multi-view channel fusion with controlled target generation, establishing a general Gen-MV sensing framework. In the proposed multi-view channel encoder, we design a multiplicative positional embedding to compensate for the impact of variable BS and UE positions on channel features. Subsequently, we implement multi-view fusion with classical architectures, and further propose an interleaved correlation learning scheme by incorporating physical information. The fused features guide the diffusion model to generate the target point cloud, and we introduce a weighted loss function to balance the spatial distribution differences of geometric shapes and EM properties of targets. The numerical results demonstrate that our proposed schemes can adapt to dynamic changes in quantities and positions of BSs and UEs, leveraging multi-view CSI to enhance environmental sensing. Ablation experiments further validate the efficacy of integrating physical priors into the GenAI framework. The proposed Gen-MV sensing framework and corresponding model designs offer a novel approach to multi-view processing in intelligent ISAC systems, and we hope it will inspire future research in this emerging field.

REFERENCES

- [1] Z. Xing, Z. Zhang, Z. Chen *et al.*, “Generative wireless sensing with multi-view channel feature aggregation,” in *IEEE Int. Symp. Pers. Indoor Mobile Radio Commun. (PIMRC)*, 2025 (submitted).
- [2] Z. Chen, Z. Zhang, and Z. Yang, “Big AI models for 6G wireless networks: Opportunities, challenges, and research directions,” *IEEE Wireless Commun.*, vol. 31, no. 5, pp. 164–172, 2024.
- [3] F. Liu, Y. Cui, C. Masouros *et al.*, “Integrated sensing and communications: Toward dual-functional wireless networks for 6G and beyond,” *IEEE J. Sel. Areas Commun.*, vol. 40, no. 6, pp. 1728–1767, 2022.
- [4] Y. Zhuo, Z. Sha, and Z. Wang, “Multibeam joint communication and radar sensing: Beamforming design and interference cancellation,” *IEEE Commun. Lett.*, vol. 26, no. 8, pp. 1888–1892, 2022.
- [5] J. A. Zhang, X. Huang, Y. J. Guo *et al.*, “Multibeam for joint communication and radar sensing using steerable analog antenna arrays,” *IEEE Trans. Veh. Technol.*, vol. 68, no. 1, pp. 671–685, 2018.
- [6] Y. Xiong, F. Liu, Y. Cui *et al.*, “On the fundamental tradeoff of integrated sensing and communications under gaussian channels,” *IEEE Trans. Inf. Theory*, vol. 69, no. 9, pp. 5723–5751, 2023.
- [7] J. Che, Z. Zhang, H. Zhang *et al.*, “A novel framework for user positioning and environment sensing during initial random access,” *IEEE Trans. Wireless Commun.*, vol. 24, no. 2, pp. 1193–1206, 2025.
- [8] Y. Jiang, F. Gao, and S. Jin, “Electromagnetic property sensing: A new paradigm of integrated sensing and communication,” *IEEE Trans. Wireless Commun.*, vol. 23, no. 10, pp. 13 471–13 483, 2024.
- [9] X. Tong, Z. Zhang, and Z. Yang, “Multi-view sensing for wireless communications: Architectures, designs, and opportunities,” *IEEE Commun. Mag.*, vol. 61, no. 5, pp. 40–46, 2023.
- [10] X. Tong, Z. Zhang, Y. Zhang *et al.*, “Environment sensing considering the occlusion effect: A multi-view approach,” *IEEE Trans. Signal Process.*, vol. 70, pp. 3598–3615, 2022.
- [11] Y. Jiang, F. Gao, S. Jin *et al.*, “Electromagnetic property sensing in ISAC with multiple base stations: Algorithm, pilot design, and performance analysis,” *IEEE Trans. Wireless Commun.*, vol. 24, no. 4, pp. 3400–3416, 2025.
- [12] Z. Xing, Z. Zhang, X. Tong *et al.*, “Physics-inspired target shape detection and reconstruction in mmwave communication systems,” in *IEEE Global Commun. Conf. (GLOBECOM)*, 2023.
- [13] Y. Cui, H. Ding, Y. Ma *et al.*, “Blockage-resilient integrated sensing and communication in mmwave networks: Multi-view collaboration and efficient task allocation,” *IEEE Trans. Mobile Comput.*, pp. 1–15, 2025.
- [14] W. Zhou, Z. Zhang, J. Che *et al.*, “Multi-view mmWave radar imaging with few measurements based on random phase shifting,” in *IEEE Veh. Technol. Conf. (VTC)*, 2024.
- [15] Z. Yu, J. Li, Q. Guo *et al.*, “Efficient direct target localization for distributed MIMO radar with expectation propagation and belief propagation,” *IEEE Trans. Signal Process.*, vol. 69, pp. 4055–4068, 2021.
- [16] J. Miguel Mateos-Ramos, C. Häger, M. Furkan Keskin *et al.*, “Model-based end-to-end learning for multi-target integrated sensing and communication under hardware impairments,” *IEEE Trans. Wireless Commun.*, vol. 24, no. 3, pp. 2574–2589, 2025.
- [17] Q. Qi, X. Chen, C. Zhong *et al.*, “Deep learning-based design of uplink integrated sensing and communication,” *IEEE Trans. Wireless Commun.*, vol. 23, no. 9, pp. 10 639–10 652, 2024.
- [18] S. Naoumi, A. Bazzi, R. Bomfin *et al.*, “Complex neural network based joint AoA and AoD estimation for bistatic ISAC,” *IEEE J. Sel. Topics Signal Process.*, vol. 18, no. 5, pp. 842–856, 2024.
- [19] Z. Liu, Q. Lan, A. E. Kalor *et al.*, “Over-the-air multi-view pooling for distributed sensing,” *IEEE Trans. Wireless Commun.*, vol. 23, no. 7, pp. 7652–7667, 2023.
- [20] Z. Xing, Z. Zhang, Z. Chen *et al.*, “VBIM-Net: Variational Born iterative network for inverse scattering problems,” *IEEE Trans. Geosci. Remote Sens.*, vol. 63, pp. 1–16, 2025.
- [21] Y. Wang, Z. Zong, S. He *et al.*, “Multiple-space deep learning schemes for inverse scattering problems,” *IEEE Trans. Geosci. Remote Sens.*, vol. 61, pp. 1–11, 2023.
- [22] Z. Chen, Z. Zhang, C. Liu *et al.*, “Towards wireless-native big AI model: Insights into its ambitions, peculiarities and methodologies,” *arXiv preprint, arXiv:2412.09041*, 2024.
- [23] G. Chi, Z. Yang, C. Wu *et al.*, “RF-diffusion: Radio signal generation via time-frequency diffusion,” in *Proc. Int. Conf. Mobile Comput. Netw. (MobiCom)*, 2024.
- [24] Z. Chen, Z. Zhang, Z. Yang *et al.*, “Channel mapping based on interleaved learning with complex-domain MLP-Mixer,” *IEEE Wireless Commun. Lett.*, vol. 13, no. 5, pp. 1369–1373, 2024.
- [25] Z. Chen, Z. Zhang, Z. Yang *et al.*, “Channel deduction: A new learning framework to acquire channel from outdated samples and coarse estimate,” *IEEE J. Sel. Areas Commun.*, vol. 43, no. 3, pp. 944–958, 2025.
- [26] Z. Chen, Z. Zhang, Z. Xing *et al.*, “Analogical learning for cross-scenario generalization: Framework and application to intelligent localization,” *arXiv preprint, arXiv:2504.08811*, 2025.
- [27] J. Wang, H. Du, D. Niyato *et al.*, “Generative AI for integrated sensing and communication: Insights from the physical layer perspective,” *IEEE Wireless Commun.*, vol. 31, no. 5, pp. 246–255, 2024.
- [28] J. Wang, H. Du, D. Niyato *et al.*, “Generative artificial intelligence assisted wireless sensing: Human flow detection in practical communication environments,” *IEEE J. Sel. Areas Commun.*, vol. 42, no. 10, pp. 2737–2753, 2024.
- [29] Y. Jiang, F. Gao, S. Jin *et al.*, “Electromagnetic property sensing based on diffusion model in ISAC system,” *IEEE Trans. Wireless Commun.*, vol. 24, no. 3, pp. 2036–2051, 2025.
- [30] J. A. Kong, *Electromagnetic wave theory*. EMW Publishing, 2008.
- [31] X. Chen, *Computational methods for electromagnetic inverse scattering*. Wiley Online Library, 2018, vol. 244.
- [32] K. Sohn, H. Lee, and X. Yan, “Learning structured output representation using deep conditional generative models,” in *Adv. Neural Inf. Process. Syst. (NeurIPS)*, 2015.
- [33] B. Mildenhall, P. P. Srinivasan, M. Tancik *et al.*, “NeRF: Representing scenes as neural radiance fields for view synthesis,” in *Proc. Eur. Conf. Comput. Vis. (ECCV)*, 2020.
- [34] Z. Chen, Z. Zhang, Z. Xiao *et al.*, “Deep learning based multi-user positioning in wireless FDMA cellular networks,” *IEEE J. Sel. Areas Commun.*, vol. 41, no. 12, pp. 3848–3862, 2023.
- [35] S. Luo and W. Hu, “Diffusion probabilistic models for 3D point cloud generation,” in *Proc. IEEE Conf. Comput. Vis. Pattern Recognit. (CVPR)*, 2021.
- [36] W. Grathwohl, R. T. Chen, J. Bettencourt *et al.*, “FFJORD: Free-form continuous dynamics for scalable reversible generative models,” in *Int. Conf. Learn. Represent. (ICLR)*, 2019.
- [37] D. Rezende and S. Mohamed, “Variational inference with normalizing flows,” in *Int. Conf. Mach. Learn. (ICML)*, 2015.
- [38] L. Dinh, J. Sohl-Dickstein, and S. Bengio, “Density estimation using real NVP,” in *Int. Conf. Learn. Represent. (ICLR)*, 2017.
- [39] Y. LeCun, L. Bottou, Y. Bengio *et al.*, “Gradient-based learning applied to document recognition,” *Proc. IEEE*, vol. 86, no. 11, pp. 2278–2324, 1998.
- [40] L. Van der Maaten and G. Hinton, “Visualizing data using t-SNE,” *J. Mach. Learn. Res.*, vol. 9, no. 11, 2008.